Supplementary Information (SI) for Journal of Materials Chemistry A.
This journal is © The Royal Society of Chemistry 2024

Supporting information for

Mechanistic insights into capacity discrepancies of conversion-type transition-metal compounds in wide-temperature-range lithium-ion batteries

Meisheng Han,[1,2] Kunxiong Zheng,[1,2] Jie Liu,[1,2] Zhiyu Zou,[1,2] Yongbiao Mu,[1,2] Hengyuan Hu,[1,2] Fenghua Yu,[1,2] Wenjia Li,[1,2] Lei Wei,[1,2] Lin Zeng,*[1,2] and Tianshou Zhao*[1,2]

[1]Shenzhen Key Laboratory of Advanced Energy Storage, Department of Mechanical and Energy Engineering, Southern University of Science and Technology, Shenzhen 518055, China

[2]SUSTech Energy Institute for Carbon Neutrality, Southern University of Science and Technology, Shenzhen 518055, China

*Corresponding Author. E-mail address: zhaots@sustech.edu.cn (T. Zhao); zengl3@sustech.edu.cn (L. Zeng)

Experimental Section

Material characterization:

The morphologies of all samples were characterized by SEM (Hitachi SU-8230). TEM equipped with EDS was performed using a Talos instrument with an acceleration voltage of 300 kV. XPS (Thermo Fisher ESCALAB Xi^+) was acquired with Al Kα (hυ = 1486.8 eV) as the excitation source. Raman spectrum was tested on a Horiba Labram HR Evolution using a 532 nm laser. XRD (D/max-2500/PC, Rigaku) was used to test the crystal structure. Elemental analyzer (Perkinelmrr 2400 Series II) and Inductively coupled plasma-atomic emission spectrometry (ICP-AES, iCAP7400 Duo MFC) were used to determine the composition of each element. TGA was tested in oxygen atmosphere using the Pyris I, PerkinElmer instrument over the temperature range of room temperature to 800 °C with a heating rate of 10 °C min^{-1}.

In-situ TEM operation process:

In situ TEM experiments were carried out on JEOL 2100F microscope working at 200 kV with a Nanofactory TEM-STM holder. The metallic Li, Li_2O, and $Fe_{1-x}S$/C served as the counter electrode, electrolyte, and working electrode, respectively. $Fe_{1-x}S$/C were adhered on a TEM Cu half-grid by electrostatic adsorption, and metallic Li was scratched by an electrochemically etched tungsten tip in a glovebox. Then, the TEM grid and the tungsten tip with metal Li were loaded onto the TEM holder and sealed in a full argon-filled bag. Before putting the tungsten tip into TEM system, it was exposured in air about 5 s to obtain Li_2O on surface of Li. In TEM, the W tip and Cu-grid were connected to the positive and negative poles of the potentiostat, respectively. Piezo-driven nanomanipulator was used to manipulate the tungsten tip with Li_2O/Li to contact the free end of the selected $Fe_{1-x}S$/C. Once they were contacted, a voltage bias of -3 or 3 V was set to initiate the lithiation or delithiation, during which TEM images, SAED patterns, EDS elemental mapping images, and movie were

recorded.

In-situ Magnetometry Experiment

This test has received the support of Professor Qiang Li from Qingdao University, and we would like to express our gratitude to Professor Qiang Li. The magnetometry test devices were assembled using flexible packaging batteries in an argon-filled glovebox at room temperature. Operando magnetometry experiments were conducted using a Quantum Design superconducting quantum interference device at -40, 25, and 60 ^{o}C. Magnetic measurements were consistently performed at an applied magnetic field of 3 T, oriented parallel to the surface of the copper foil. Simultaneously, operando magnetic measurements were performed in conjunction with electrochemical workstation in the form of testing CV curves at 0.5 mV s^{-1} from -40 to 60 ^{o}C. To extract the relevant magnetic data, linear magnetic background signals originating from other components of the cell assembly were meticulously subtracted from the total magnetic moment.

Electrochemical measurements:

Half-cell assessment: CR2032-type coin cells were assembled. The working electrodes were composed of active materials, acetylene black, and polyvinylidene fluoride at a mass ratio of 8:1:1. The obtained electrodes were dried under vacuum at 90 °C for at least 12 h. while lithium metal piece was served as the counter/reference electrode, and Celgard 2400 was used as separator. The electrolyte (1 M $LiPF_6$ in ethylene carbonate, ethyl methyl carbonate (EMC), and methyl propionate (MP) with 5% fluoroethylene-carbonate) is commercially accessible, in which EMC and MP have high freezing points of -53 and -80 ^{o}C, respectively, which can be used as excellent low-temperature electrolyte, as reported previously (Angew. Chem. Int. Ed., 2019, 58, 18892-18897; Adv. Funct. Mater., 2021, 31, 2009397). The mass loading of active materials is around 1.20 mg cm^{-2}. The electrochemical performance was evaluated using a Neware battery test system (Shenzhen, China) at temperatures of -40, 25, and 60 ^{o}C. EIS with frequency ranges of 10^{5} to 10^{-2} Hz were conducted

using a CHI 760D electrochemical workstation (Shanghai CH Instruments Co., China).

DFT calculations:

We have employed the Vienna ab initio simulation package (VASP) [1,2] to perform all DFT calculations within the generalized gradient approximation (GGA) using the Perdew-Burke-Ernzerhof (PBE) [3] formulation. We have chosen the projected augmented wave (PAW) potentials [4,5] to describe the ionic cores and take valence electrons into account using a plane wave basis set with a kinetic energy cutoff of 450 eV. Partial occupancies of the Kohn-Sham orbitals were allowed using the Gaussian smearing method and a width of 0.05 eV. The electronic energy was considered self-consistent when the energy change was smaller than 10^{-5} eV. A geometry optimization was considered convergent when the force change was smaller than 0.05 eV/Å. Grimme's DFT-D3 methodology [6] was used to describe the dispersion interactions. The Brillourin zone was sampled with a gamma-centered grid 2 × 2 × 1 through all the computational process. [7] A climbing image nudged elastic band (CI-NEB) method was used to locate the transition states with the same convergence standard.

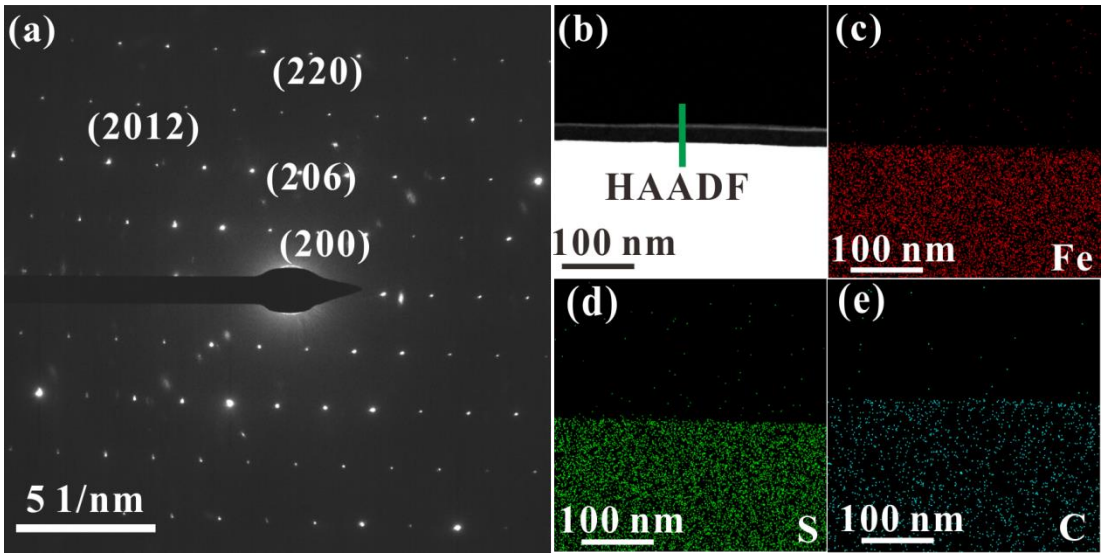

Figure S1. TEM characterizations of the $Fe_{1-x}S/C$: (a) SAED pattern, (b) High-angle annular dark field (HAADF) image and (c-e) corresponding mapping images.

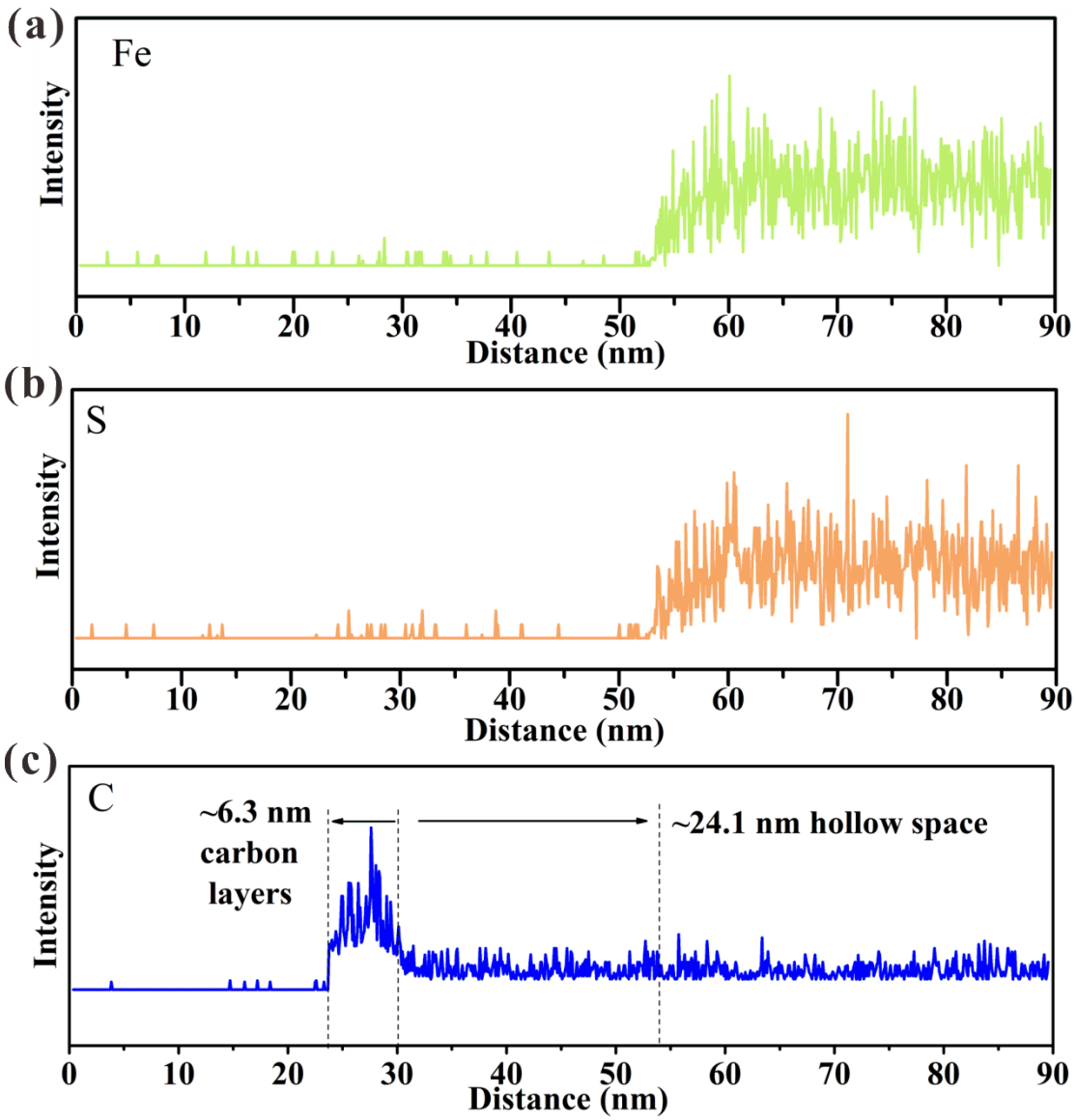

Figure S2. EDS line scan results of (a) Fe, (b) S, and (c) C elements from the green line in Figure S2b.

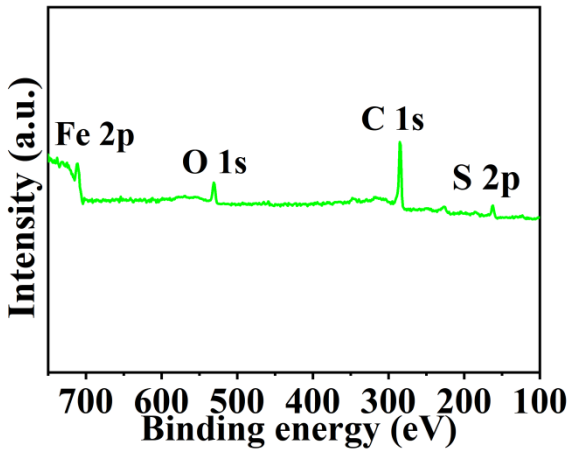

Figure S3. XPS survey peak of $Fe_{1-x}S/C$.

Table S1. Fitting results of XPS survey spectrum of the sample.

Samples	Fe (at%)	O (at%)	S (at%)	C (at%)
$Fe_{1-x}S/C$	17.63	4.24	19.60	58.53

Table S2 The elemental analysis results of the obtained samples.

Sample	Fe (wt%)	S (wt%)	C (wt%)	O (wt%)
$Fe_{1-x}S/C$	57.202	36.431	6.235	0.132

The C, N, O, and S contents in the composites were measured using O/N/H and C/S elemental analyzers. The Fe contents in the composites can be calculated by the difference between 100 wt% and the total mass percentage of S/C/O. Inductively coupled plasma-atomic emission spectrometry (ICP-AES) was further used to determine the content of Fe, which is about 57.326wt%, basically consistent with the results of elemental analysis (Table S2). Based on the elemental analysis and ICP-AES results, it can be concluded that the atomic ratio of Fe and S is about 0.9, which is in accordance with the XPS result (Table S1).

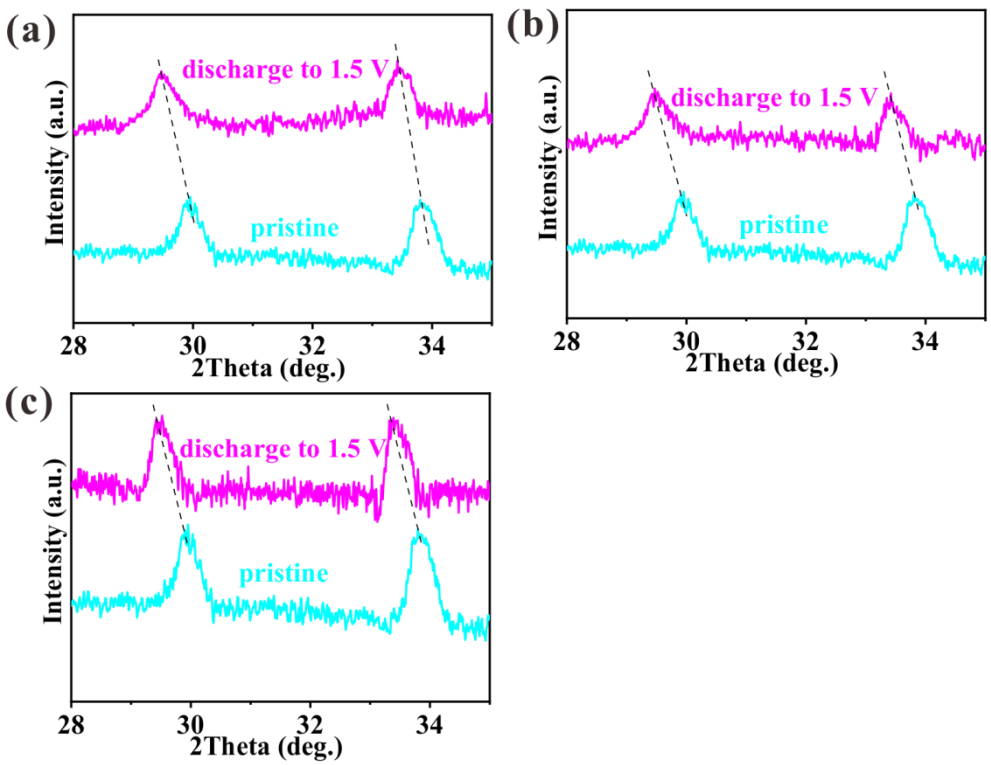

Figure S4. Ex-situ XRD patterns of $Fe_{1-x}S$/C electrodes between 28 and 35°: (a) at -40 °C; (b) 25 °C; (c) 60 °C.

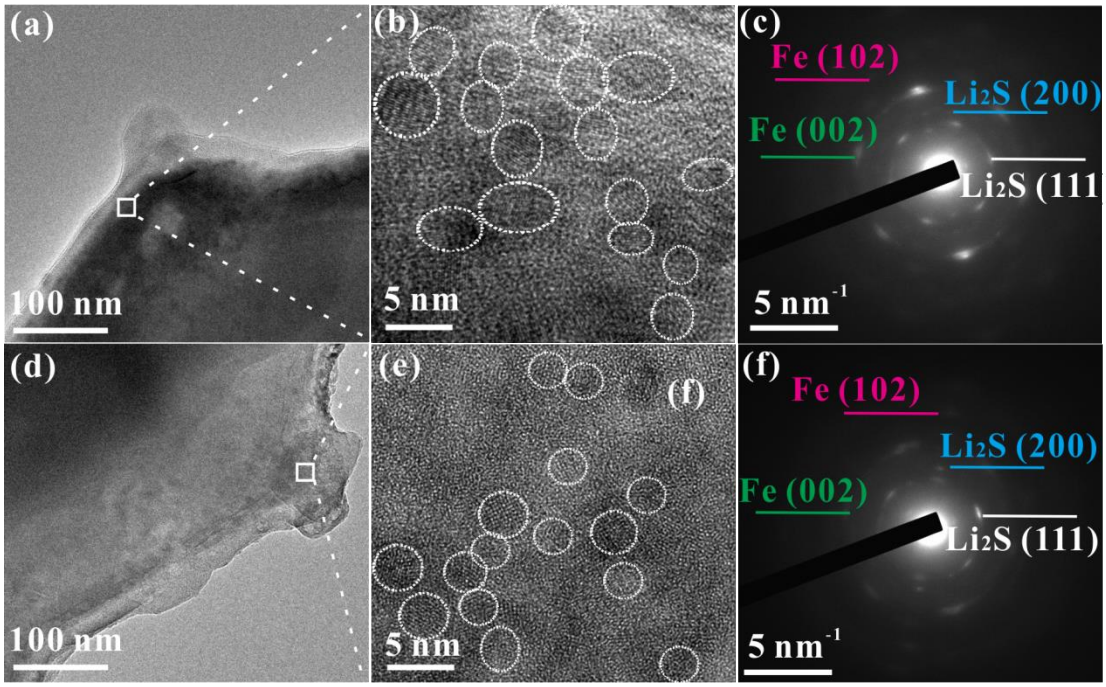

Figure S5. Ex-situ TEM characterizations of $Fe_{1-x}S/C$ after discharging to 0.01 V at -40 ºC: (a,b) TEM images and (c) corresponding SAED pattern; Ex-situ TEM characterizations of $Fe_{1-x}S/C$ after discharging to 0.01 V at 60 ºC: (d,e) TEM images and (f) corresponding SAED pattern.

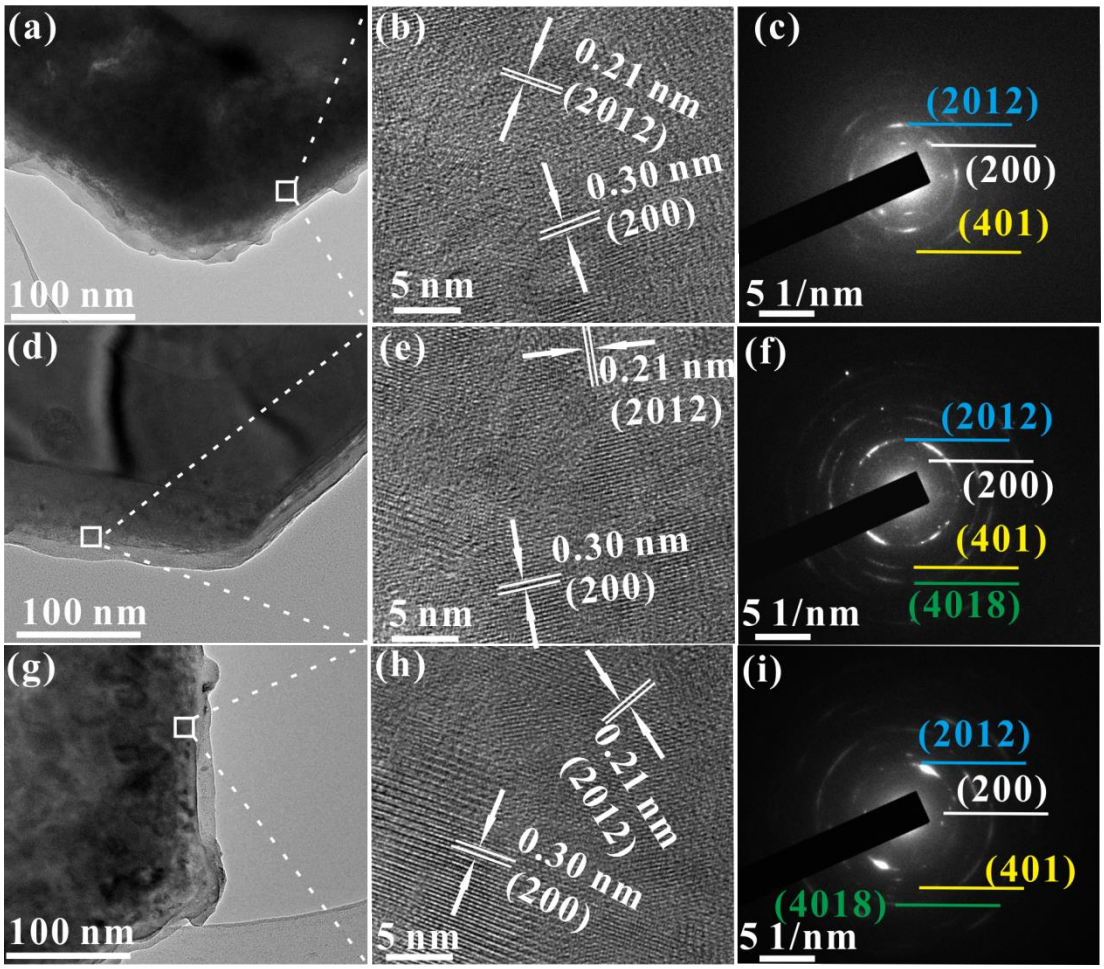

Figure S6. Ex-situ TEM characterizations of $Fe_{1-x}S$/C electrodes after charging to 3.0 V: (a-c) TEM images (a,b), and the corresponding SAED pattern (c) at a temperature of -40 ºC; (d-f) TEM images (d,e), and the corresponding SAED pattern (f) at a temperature of 25 ºC; (g-i) TEM images (g,h), and the corresponding SAED pattern (i) at a temperature of 60 ºC. Images b and c, e and f, and h and i are obtained from the marked white rectangles in images a, d, and g, respectively.

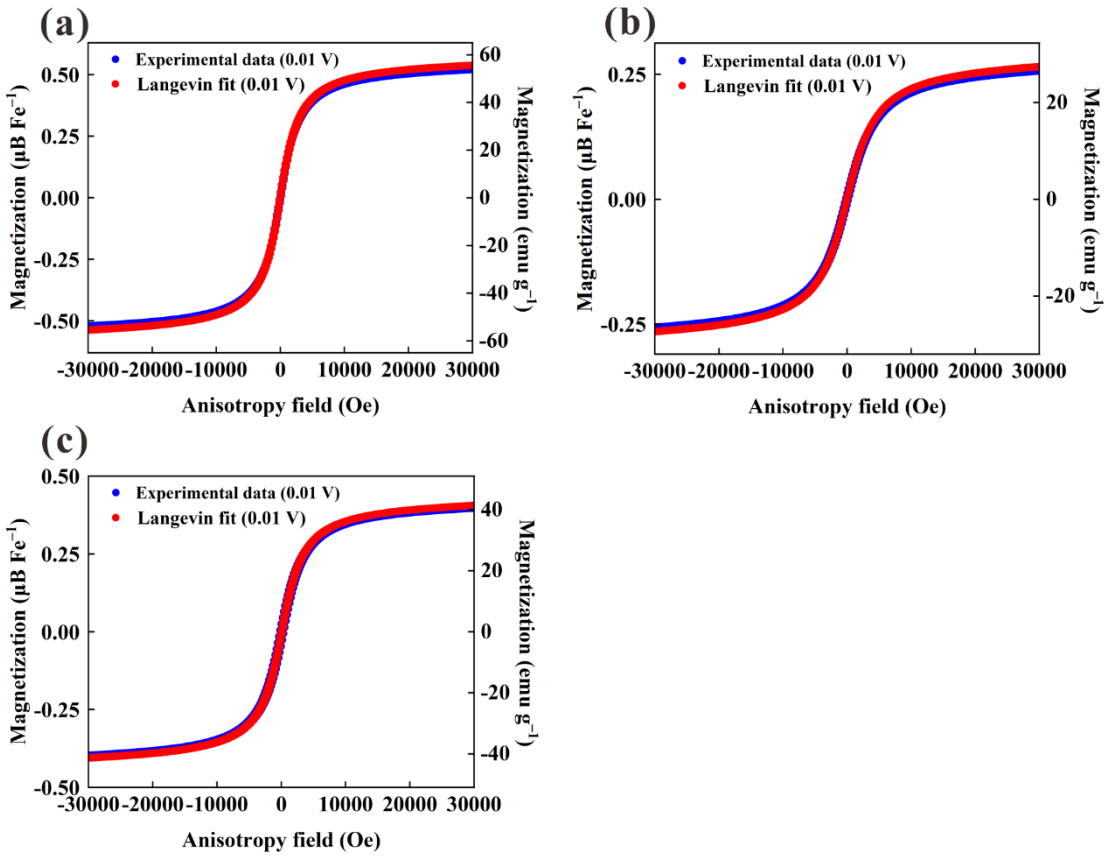

Figure S7. Magnetic hysteresis curves of the $Fe_{1-x}S$/C electrodes after discharging to 0.01 V (blue points), and the corresponding Langevin fitting curves for the latter (red points) at (a) -40 °C, (b) 25 °C, and (c) 60 °C.

We disassembled the battery at 0.01 V and ex-situ measured the magnetic hysteresis. The magnetization of superferromagnetic particles follows a Langevin function:

$$M(H,T) = M_0\mathcal{L}(\mu_P H/kT)$$

where $\mathcal{L}(x) = \coth x - (1/x)$ and μ_P is the magnetic moment per particle. Fitting our measured data at 233, 298, and 333 K to the Langevin function, we found $\mu_P \approx 2012\ \mu_B$ across the wide temperature range. Considering 2.22 μ_B per Fe atom, an average particle diameter of 2.73 nm could be deduced.

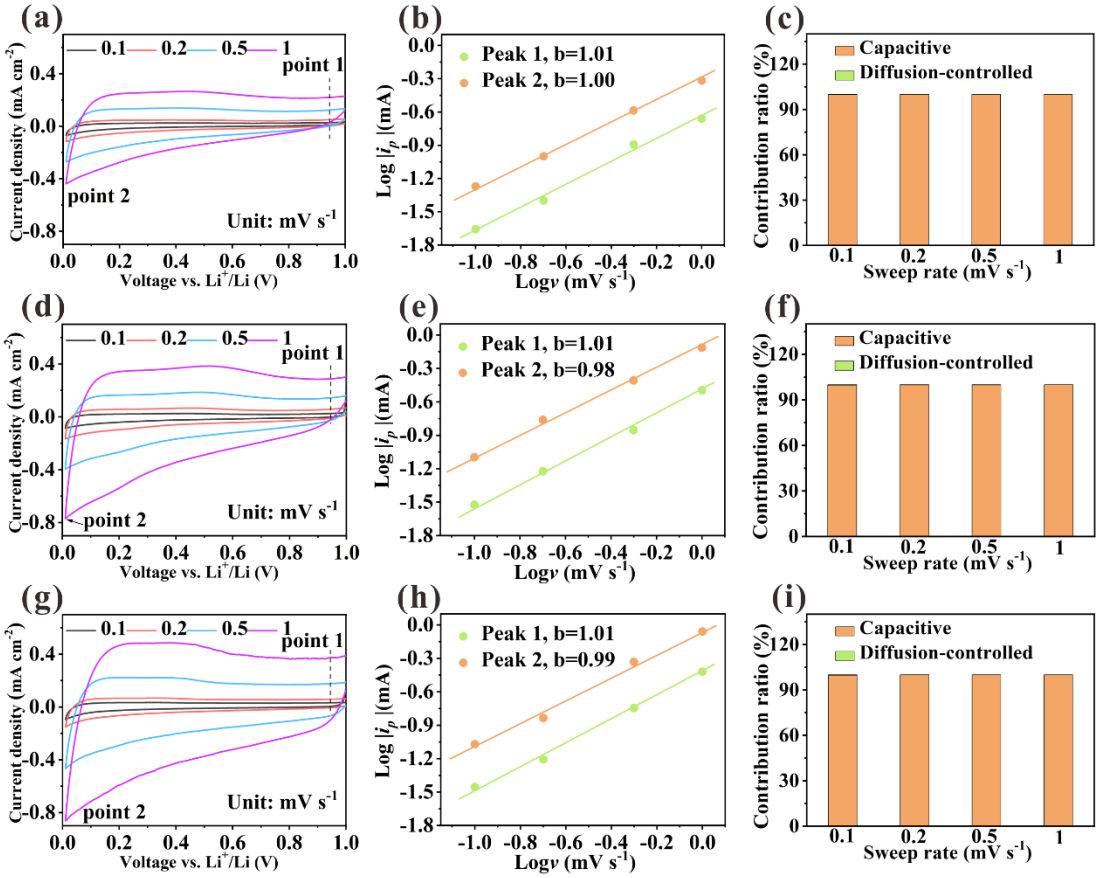

Figure S8. Kinetic analysis of $Fe_{1-x}S$/C electrode at (a-c) -40 °C, (d-f) 25 °C, and (g-i) 60 °C. (a, d, g) CV curves at different scanning rates, (b, e, h) Logi_p *vs* Log$v$, (c, f, i) pseudocapacitive contribution percentages.

To comprehend the electrochemical kinetics and quantitative analysis of $Fe_{1-x}S$/C electrodes from 0.01 to 1 V over a wide temperature range in detail, CV profiles at various scan rates (0.1-1.0 mV s^{-1}) are measured. Apparently, the CV profiles exhibit rectangular shape during charge and discharge processes at different scanning rates (Figure S8a,d,g), which further indicates that capacitive-controlled process is dominant. The peak current (i) and the scan rate (v) obey the following equation.

$$i = av^b$$

where a and b are empirical constants. Especially, the b-value of 0.5 belongs to a complete diffusion-controlled behavior and the b-value of 1.0 indicates an absolute capacitive-controlled process. The b-values of the marked points 1 and 2 in both cathodic and anodic processes at -40 (Figure S8b), 25 (Figure S8e), and 60 (Figure S8h) °C are approximately equal to 1, which fully proves a complete capacitive-controlled

process at the voltages of 0.01-1 V. As calculated in Figure S25c,f,i, the $Fe_{1-x}S$/C electrodes show ~100% capacitive contribution at various scanning rates over a wide temperature range. The above results further demonstrate that spin-polarized surface capacitance effect plays a total dominant role on ion storage and transport between 0.01 to 1 V from -40 to 60 ^{o}C.

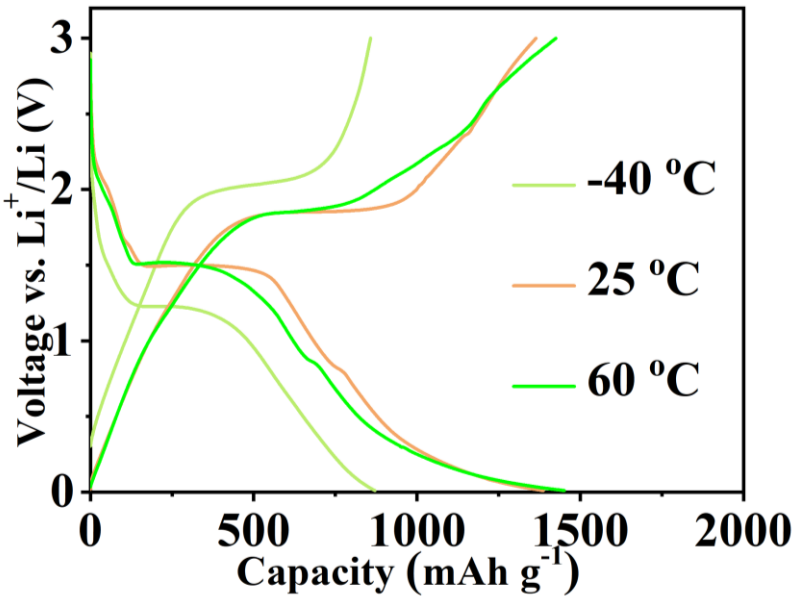

Figure S9. The second charge and discharge curves at 0.1 A g^{-1} of $Fe_{1-x}S$/C electrodes at different temperatures

Table S3. The specific voltage range, capacity contribution, and capacity contribution ratio of insertion reaction, conversion reaction, and space charge formation of $Fe_{1-x}S$/C electrodes at -40 °C. The results are from in-situ magnetometry (Figure 4d) and charge/discharge curve (Figure 5a). open circuit voltage-OCV

Ion storage stages	Insertion	Conversion	Space charge
Voltage range (V)	OCV-1.43	1.43-0.60	0.60-0.01
Capacity contribution (mAh g^{-1})	66.7	547.9	256.8
Capacity contribution ratio (%)	7.0	62.9	30.1

Table S4. The specific voltage range, capacity contribution, and capacity contribution ratio of insertion reaction, conversion reaction, and space charge formation of $Fe_{1-x}S$/C electrodes at 25 ^{o}C. The results are from in-situ magnetometry (Figure 4e) and charge/discharge curve (Figure 5b). open circuit voltage-OCV

Ion storage stages	Insertion	Conversion	Space charge
Voltage range (V)	OCV-1.52	1.52-0.92	0.92-0.01
Capacity contribution (mAh g^{-1})	119.8	495.4	590.7
Capacity contribution ratio (%)	9.9	41.1	49.0

Table S5. The specific voltage range, capacity contribution, and capacity contribution ratio of insertion reaction, conversion reaction, and space charge formation of $Fe_{1-x}S$/C electrodes at 60 °C. The results are from in-situ magnetometry (Figure 4f) and charge/discharge curve (Figure 5c). open circuit voltage-OCV

Ion storage stages	Insertion	Conversion	Space charge
Voltage range (V)	OCV-1.53	1.53-1.01	1.01-0.01
Capacity contribution (mAh g^{-1})	125.6	491.8	833.8
Capacity contribution ratio (%)	8.7	33.9	57.5

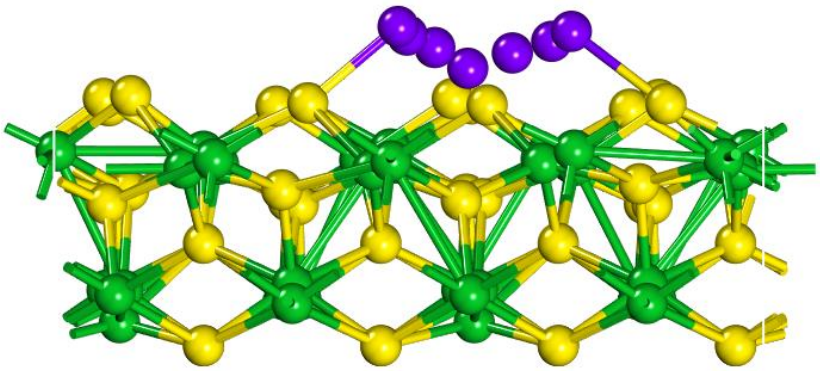

Figure S10. Side view of configurations of lithium migration paths.

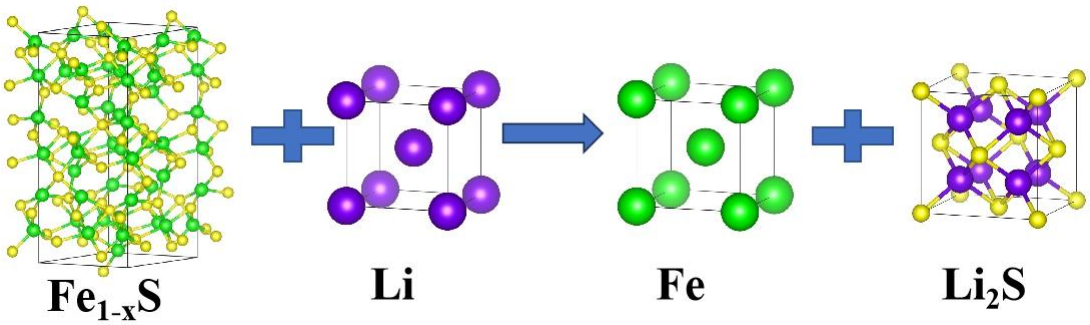

Figure S11. Atomic configurations in the calculation of the Gibbs free energy required for conversion reaction.

Table S6. Magnetization of $Fe_{1-x}S$/C electrodes in the second cycle from different voltage points in Figure 4d,e,f at -40, 25, and 60 ºC, and their corresponding magnetization values in these voltage points are marked as M_{Vx} (x=1, 2, and 3), where V1: Cut-off voltage of conversion reaction; V2: 0.01 V; V3: Starting-voltage of oxidation reaction; M_{V1-V2}: The difference value between M_{V1} and M_{V2}; M_{V3-V2}: The difference value between M_{V3} and M_{V2}.

M_{Vx} (emu g^{-1})	M_{V1}	M_{V2}	M_{V3}	M_{V1-V2}	M_{V3-V2}
-40 ºC	73.2	55.3	83.2	17.9	27.9
25 ºC	63.1	41.1	82.2	22.0	41.1
60 ºC	62.6	27.7	74.9	34.9	47.2

References

[1] Kresse, G.; Furthmüller, J. Efficiency of Ab-Initio Total Energy Calculations for Metals and Semiconductors Using a Plane-Wave Basis Set. Comput. Mater. Sci. 199, 6, 15−50.

[2] Kresse, G.; Furthmüller, J. Efficient Iterative Schemes for Ab Initio Total-Energy Calculations Using a Plane-Wave Basis Set. Phys. Rev. B 1996, 54, 11169−11186.

[3] Perdew, J. P.; Burke, K.; Ernzerhof, M. Generalized Gradient Approximation Made Simple. Phys. Rev. Lett. 1996, 77, 3865−3868.

[4] Kresse, G.; Joubert, D. From Ultrasoft Pseudopotentials to the Projector Augmented-Wave Method. Phys. Rev. B 1999, 59, 1758-1775.

[5] Blöchl, P. E. Projector Augmented-Wave Method. Phys. Rev. B 1994, 50, 17953−17979.

[6].Grimme, S.; Antony, J.; Ehrlich, S.; Krieg, H. J. Chem. Phys. 2010, 132, 154104.

[7].H. J. Monkhorst and J. D. Pack, Phys. Rev. B, 1976, 13, 5188-5192.